Temperature estimation and slip-line force analytical models for the estimation of the radial forming force in the RARR process of flat rings

Temperature estimation and slip-line force analytical models for the estimation of the radial forming force in the RARR process of flat rings

Luca Quagliato, Guido A. Berti

www.elsevier.com/locate/ijmecsci

PII: S0020-7403(16)30406-4
DOI: http://dx.doi.org/10.1016/j.ijmecsci.2017.02.008
Reference: MS3593

To appear in: *International Journal of Mechanical Sciences*

Cite this article as: Luca Quagliato and Guido A. Berti, Temperature estimation and slip-line force analytical models for the estimation of the radial forming force in the RARR process of flat rings, *International Journal of Mechanical Sciences* http://dx.doi.org/10.1016/j.ijmecsci.2017.02.008

Temperature estimation and slip-line force analytical models for the estimation of the radial forming force in the RARR process of flat rings

Authors (in this order): Luca Quagliato, Guido A. Berti

Affiliation (both authors):

Department of Management and Engineering, University of Padua, Stradella San Nicola 3, 36100, Vicenza.

Corresponding author details:

Luca Quagliato

Department of Management and Engineering

University of Padua

Tel: +39 0444 998724

Fax: +39 0444 998889

Abstract

In this study, a mathematical model for the prediction of the temperature evolution in the ring during the radial-axial ring rolling process is developed and used, together with the authors' previous results, to determine analytically the flow stress of the material during process. These results, combined with Hill's slip-line field solution adapted to the RARR process, allow a fast and reasonably precise calculation of the radial forming force, a key parameter at the preliminary stage of the process design. The approach is validated by applying the proposed model to a case available in the literature and comparing the analytical results with those of the laboratory experiment and FEM simulation. Following the successful comparison, the models were applied to a large variety of flat rings, comparing analytical predictions with the results of FEM simulations. The accuracy of the analytical calculation and the reliability of the proposed models, for different ring configuration and process parameters, are presented and discussed.

Key words: ring rolling, temperature estimation, slip-line, force prediction, FE analysis.

1. Introduction

Radial-axial ring rolling (RARR) is a multi-stage manufacturing technique that allows the production of seamless and near-net-shape forgings made from various materials and with various shapes [1]. The ring rolling technique has evolved over 150 years with significant research work over the last 40 years [2]. In recent years, the introduction of FEM simulation has radically widen the possibilities of investigation and improvement in the RARR process. However, the development of algorithms capable of reducing the number of FEM simulations required to obtain the best configuration of set-up parameters would still be very helpful. This is particularly requested in the industrial applications in order to reduce the time required for the design of the process. The design phase of many manufacturing processes, including the RARR process, must take into account technological constraints, such as the maximum forming force of the available machines. For this reason, an algorithm capable of quickly calculating the process forces, and hence allowing the process planner to explore many different combinations of process parameters, would be very useful in both industrial and research environments.

In the last 70 years, much effort has been spent in the development of different techniques for calculating the forces in the RARR process. These include the FE methodology by Zhou et al. [1] and by Guo et al. [3]; the SLAB method by Parvizi et al. [4]; the upper bound analysis by Parvizi et al. [5]; and the slip-line method by Hawkyard et al. [6] and by Mamalis et al. [7]. If properly set-up, the FE methodology can give a precise estimation of the process forces but it is a very time-consuming technique, especially if many different combinations of process parameters have to be explored. The upper-bound method can overestimate the force prediction since only the velocity field is taken into account. On the other hand, if the velocity field is neglected and only the stress field is considered, the calculation results in an underestimation of the process forces.

In this context, the aims of the present research work are twofold. The first is the development of an algorithm capable of predicting the average temperature evolution resulting from the combination of conductive, convective and radiant heat exchange in the ring during the process. This area has not yet been fully explored in the literature. The second aim is to use the resultant temperature prediction, together with the authors' previous results related to geometry, strain and strain rate estimation [8, 9] to calculate the flow stress of the material at each round of the process. This allows the calculation of the radial forming force by adapting the Hill's slip-line solution developed for flat indenters to the RARR process [10].

The analysis performed by Hawkyard et al. [6], based on the Hill's slip-line solution for the indentation of a slab by opposite flat indenters [10], is extended here to the hot ring rolling process for a range of rings having final diameters from 650 mm to 2400 mm. In order to understand the influence of the ring section geometry on the quality of the force prediction, three cases with different ratios between final height and final thickness of the ring have been analyzed for each tested ring diameter.

The results of the temperature estimation show good agreement with the output of the FEM simulation, proving the reliability of the assumptions formulated for the description of the contact between the ring and the tools. Moreover, the calculation of the radial forming force will show how the slip-line solution reasonably approximates the FEM simulation for a wide range of rings and ring sections, but loses accuracy if the final diameter of the ring is sufficiently small, due to the difference of the contact zone with respect to the flat indenter condition. Since the average mandrel feeding speed has also shown to influence the forming force, as also anticipated by Ryoo et al. [11], the correlation between force estimation and average mandrel feeding speed is explored allowing a better interpretation of the results of the proposed approaches for the calculation of the radial forming force.

2. Analytical model for the estimation of the temperature evolution in the ring

In order to calculate the process forces in the mandrel-main roll deformation gap, the geometry of the ring section undergoing the deformation, its effective plastic strain, effective strain rate and temperature are required. Most of these data can be calculated from the initial and final shape of the ring and from the motion laws applied to the main-roll, the mandrel and the axial rolls, as detailed in [8] and [9]. As concerns the estimation of the temperature of the ring during the process, a laborious and complicated model, as suggested but not verified in [12], is out of the scope of this paper. For this reason, in this research work, the plastic deformation heat and the friction-caused heat are neglected. The simplified analytical model proposed in this paper takes in account conductive, convective and radiant heat exchange among the ring, the tooling system and the environment and allows estimating the temperature evolution in the ring during the process, with a limited error. Moreover, the proposed algorithm can be implemented easily in various software packages or calculation worksheets, making it possible to include it inside already existing codes and programs.

The purpose of this section is to define three different lumped heat exchange models: a conductive one for the mandrel-main roll deformation gap, a conductive one for the axial rolls deformation gap and a mixed convective-radiant heat exchange model applied to the whole ring (Fig. 1). These models will be applied following this order, assuming that: the conductive heat exchange between ring and mandrel/main roll acts only during the deformation in this gap; the conductive heat exchange between ring and axial rolls acts only during the deformation in this gap; and that the heat exchange between the ring and the environment acts only when the ring rotates between these two deformation gaps. The results of the calculation will be compared with the results of FE simulations, demonstrating the reliability of the proposed approach.

2.1 Conductive heat exchange model for the mandrel-main roll deformation gap

In this section, as first, some consideration about the contact geometry between ring and tools will be derived and later utilized as input parameters for the temperature model, where the contact area plays an important role in the prediction of the temperature. Considering that both mandrel and main-roll radii are normally greater than the projection of the contact arc between tools and ring, authors have chosen to assume a common projection for the contact arc on the x-axis, in terms of L_C, calculated utilizing Eq. (1) [13], as shown in Fig. 2. Each ring section enters the deformation gap with a specific initial thickness s_0 and exits it with a final one s_1. The size of the section is determined by its position in the ring and on the motion laws of the tools of the ring rolling mill.

$$L_C = \sqrt{\frac{2\Delta h}{\left(\frac{1}{R_S}\right)+\left(\frac{1}{R_M}\right)+\left(\frac{1}{R}\right)-\left(\frac{1}{r}\right)}} \tag{1}$$

R_S and R_M are the radii of main-roll and mandrel respectively, whereas r and R are the average inner and outer radius of the ring section undergoing the deformation, respectively.

Based on the values of L_C and r, or R, the contact angle α_M on the mandrel side, or α_S on the main-roll side, referred to the center of inner, or outer, radius of the ring, Fig. 2, can be calculated as in Eq. (2). Being the algorithm applicable to both contact zones, the following procedure will be derived considering the mandrel-inner ring radius contact zone, since it can easily be extended to the main roll-outer ring radius zone by substituting the relevant parameters.

$$\alpha_M = \arcsin\left(\frac{L_c}{r}\right) \tag{2}$$

The time t_i required for a generic section of the ring to complete i-round can be reasonably approximated as the ratio between the external length of the ring at the end of previous i-1 round and the tangential speed of the main roll [8], assuming no slipping between ring and main-roll.

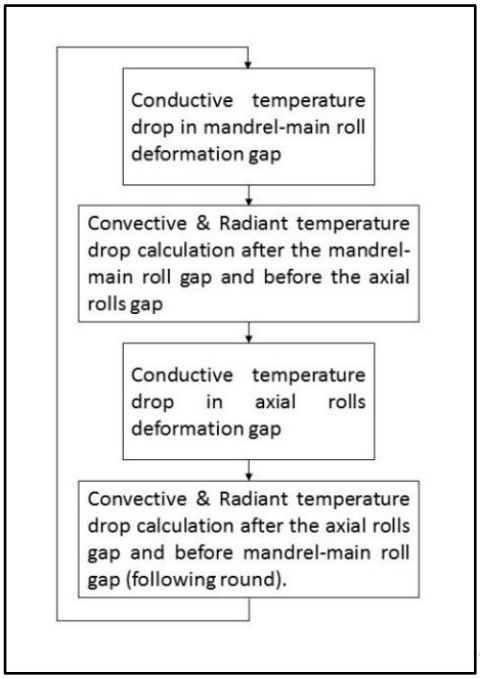

Figure 1 - Heat exchange models flow chart

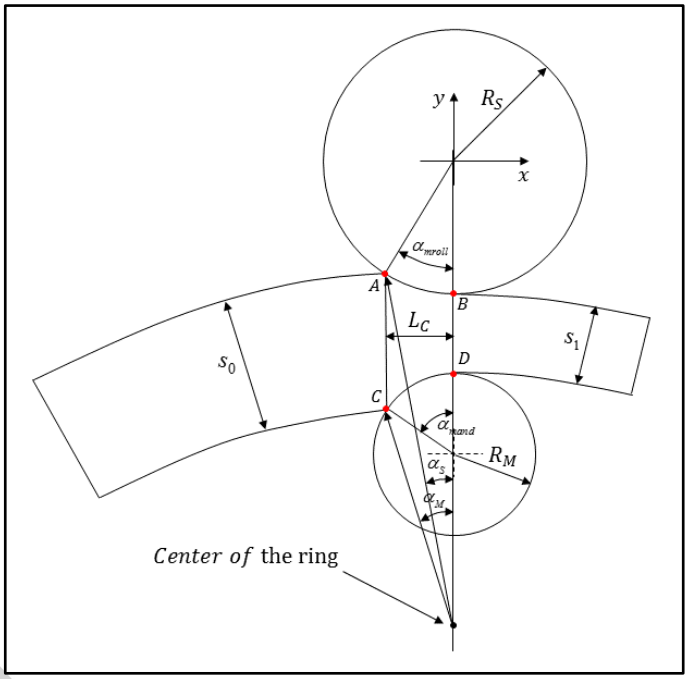

Figure 2 - Mandrel-main roll deformation gap

As the ring has completed its round after a rotation of 2π in a time t_i, the total contact time t_M between the ring and the mandrel, in the generic round, can be estimated as in Eq. (3) using the vertex angle obtained from Eq. (2).

$$t_M = t_i \frac{\alpha_M}{2\pi} \tag{3}$$

The calculation of the heat exchange area between ring and mandrel is not straightforward because the ring is continuously changing its geometry (inner radius of the ring) and it can not be assumed as an arc of circumference. Looking at the instantaneous contact area on the mandrel side, the major advantage is that it is arc of circumference with a constant radius R_M and an angle α_{mand} referred to the center of the mandrel calculated as in Eq. (4). The contact exchange area, A_{mand}, calculated as part of the mandrel surface being instantaneously in contact with the ring can be derived accordingly in Eq. (5), where $\bar{h}$ is the average height of the portion of the ring undergoing the deformation.

$$\alpha_{mand} = \arcsin\left(\frac{L_c}{R_M}\right) \tag{4}$$

$$A_{mand} = \alpha_{mand} \cdot R_M \cdot \bar{h} \tag{5}$$

The product between contact time and contact area is correct if both these terms are evaluated in the same reference and for this reason it is necessary to introduce a sort of transmission ratio η_M calculated as the ratio between the contact area measured on the mandrel surface A_{mand} and the contact area measured on the inner surface of the not deformed ring $A_{mand,undef}$, leading to Eq. (6).

$$\eta_M = \frac{A_{mand}}{A_{mand,undef}} = \frac{\alpha_{mand} \cdot R_M \cdot \bar{h}}{\alpha_M \cdot \bar{h} \cdot r} \tag{6}$$

Similar considerations can be repeated using the parameters relevant to the main roll-outer ring radius and applying them to equations from (2) to (6), the following parameters can be derived: α_S, t_S, α_{mroll}, A_{mroll}, η_S. In a complete round of the ring, the total inner surface of the not deformed ring, $A_{in} = 2\pi r\bar{h}$, has been in contact with the mandrel for a time t_M whereas the total outer surface of the not deformed ring, $A_{out} = 2\pi R\bar{h}$, has been in contact with the main roll for a time t_S.

Hence, considering the area related to the inner radius, $A_{in} = 2\pi r\bar{h}$, and that related to the outer radius, $A_{out} = 2\pi R\bar{h}$, the weighted product between heat exchange area and time to be used in the heat exchange equation (8) can be calculated as in (7), where half of the volume of the ring is considered. Subscripts "j" and "j-1" indicate the actual step and the previous one in the calculation.

$$2A_{equiv,M} \cdot t_{equiv,M} = A_{in} \cdot t_M \cdot \eta_M + A_{out} \cdot t_S \cdot \eta_S \tag{7}$$

$$T_{mand,i} = \left(T_{j-1} - T_T\right) \cdot \exp\left(\frac{2A_{equiv,M} \cdot t_{equiv,M} \cdot HTC}{C\rho V}\right) \tag{8}$$

In Eq. (8), T_T is the tools temperature (considered as a constant value throughout the process), C is the specific heat capacity of the material, ρ is the density of the material, HTC is the conductive heat transfer coefficient and V the volume of the ring (considered as a constant thanks to the volume conservation principle in plastic deformation). Moreover, as previously anticipated and shown in Fig. 1, since the estimation of the temperature is based on each half round of the ring rotation, in Eq. (8), only half of the volume of the ring is considered. The model takes then into account only the portion (half) of the ring exited from the axial rolls gap and entering the mandrel-main roll gap.

In conclusion of this section, if the ring is considered to rotate clockwise, the value of T_{j-1} will be the temperature resulting from the application of the mixed convective-radiant heat exchange model (detailed below) to the half ring between the axial rolls gap and the mandrel-main roll gap. $T_{mand,i}$ can therefore be considered as the average temperature of the ring for the i-round of the process.

2.2 Calculation of the temperature evolution in the axial rolls deformation gap

Since the contact zone between axial rolls and ring differs from that for the mandrel-main roll gap described in the previous section, a new expression to formulate the conductive heat exchange in the axial rolls deformation gap is required. The real contact surface between the ring and the axial roll is quite complex to evaluate due to the conical surface of the axial rolls deforming the flat surface of the ring then, to clarify this point, some consideration must be firstly pointed out.

The total variation of the ring height generated by the axial rolls is Δh and, for the symmetry of both the geometry and the constraints, is considered to be equally distributed on the upper and lower surfaces of the ring, resulting in $\Delta h/2$ for both sides. This height variation is gradually imposed by the geometry of the cone in contact with the flat surface of the ring and the height distribution varies moving from the onset toward the exit of the axial rolls deformation gap. Moreover, if the height variation is evaluated along the z-direction, Fig. 3, the contact arc between ring and axial roll will result in portion of ellipses, whereas, if it is evaluated along the direction orthogonal to the axis of the axial roll, it will result in an arc of circumference. Authors' have chosen to adopt this second strategy, projecting the height reduction $\Delta h/2$ onto the direction orthogonal to the axis of the axial rolls and calculating the relevant projection Δh_{INCL} as in Eq. (9), where θ is the vertex semi angle of the axial roll. Thus, the contact arc between the upper, and lower, surfaces of the ring and the axial rolls shall be considered as an arc of circumference.

For each slice of the ring, the algorithm proposed in [8] enables to calculate the height of the slice at each round of the process. The height of the slice before entering the axial rolls gap, h_{in}, corresponds to the height of the considered slice at the end previous round, whereas the height of the slice after exiting from the axial rolls gap, h_{out}, corresponds to the height at the current round. Hence, the variation of the height of the slice when it passes in the axial roll gap can be calculated as $\Delta h = h_{in} - h_{out}$.

$$\Delta h_{INCL} = \frac{1}{2}\frac{\Delta h}{\cos\theta} \tag{9}$$

As shown in Fig. 3, the two extremum points of contact between the axial roll and the ring are **P1** and **P2**. The corresponding radii on the axial roll are R_{oc} and R_{ic} which are measured, according to (10) and (11), as the distance between the contact point between ring and cone and the axis of the cone.

$$R_{ic} = (L - s)\sin\theta \tag{10}$$

$$R_{oc} = L\sin\theta \tag{11}$$

For point **P1** this distance from the virtual vertex of the cone is denoted as L whereas, for **P2**, it is $L - s$; for large rings L is usually kept constant to its initial value L_0 whereas different rules can be adopted for small rings, where L is allowed to vary during the process.

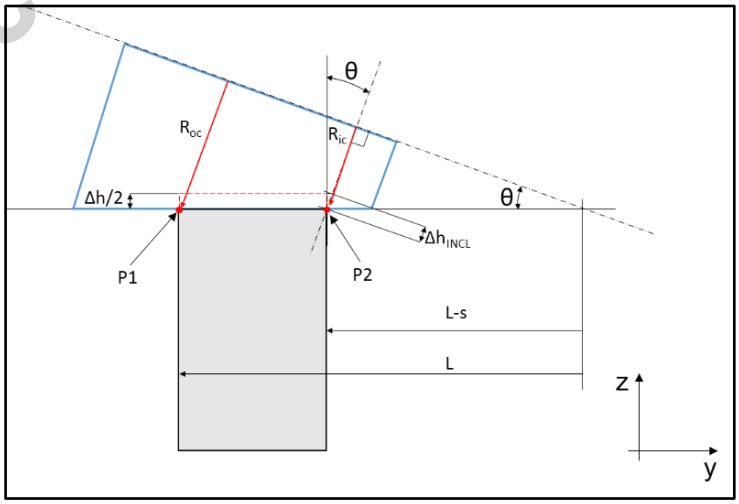

Figure 3 - Contact between ring and axial rolls (side view)

The curved line resulting from the intersection between the conical surface and the inner (or outer) cylindrical surface of the ring is quite complex to be exactly determined. Thanks to the small values of Δh respect to ring and axial rolls dimensions, the contact arc between ring and axial rolls can be calculated on a plane orthogonal to the axis of the axial roll and passing through **P1**, or **P**2. For this circular arc, considering (10) and (11), the center angle related to the contact radius R_{ic} is calculated as in Eq. (12), Fig. 4a, and the corresponding length of the contact arc l_1, at the inner radius, is straightforwardly defined by Eq. (13), as shown in Fig. 4a. This formulation can be easily extended to the outer contact radius R_{oc} substituting the relevant parameters and leading to the calculation of l_2.

$$\alpha_{\mathrm{C,int}} = \arccos\left(\frac{R_{ic} - \Delta h_{INCL}}{R_{ic}}\right) \tag{12}$$

$$l_1 = \alpha_{C,\mathrm{int}} \cdot R_{ic} \tag{13}$$

Since this circumference arcs pertain both to the axial roll and to the cylindrical surface of the ring, their length l_1 and l_2, measured on the axial roll as just explained, are also relevant for the ring.

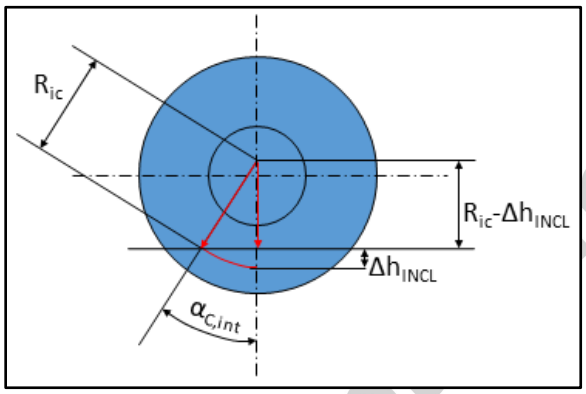

Figure 4.a - Contact between ring and axial rolls (front view)

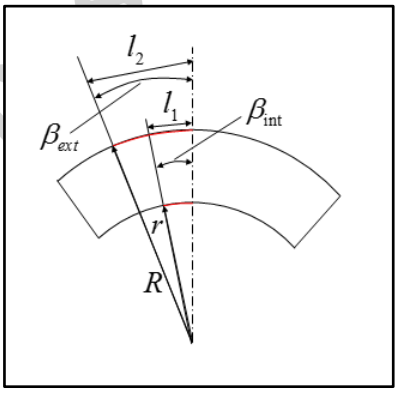

Figure 4.b - Contact between ring and axial rolls (top view)

As shown in Fig. 4b, referring to the inner and outer radius of the ring, the two angles related to the projection of l_1 and l_2 on the x-y plane, can be estimated as in (14).

$$\beta_{\mathrm{int}} = \frac{\alpha_{\mathrm{C,int}} \cdot R_{ic}}{r} \quad ; \quad \beta_{ext} = \frac{\alpha_{C,\mathrm{out}} \cdot R_{oc}}{R} \tag{14}$$

This last step leads to the first calculation of the projection of contact area on the x-y plane, (15), where $\bar{s}$ is the average thickness of the portion of the ring undergoing the deformation. As shown in (16), the contact time t_C is given by the time t_i to complete the current round multiplied by the ratio between the projected contact surface, Eq. (15), and the whole top surface of half ring.

$$A_C = \left(\beta_{\mathrm{int}} \cdot r + \beta_{ext} \cdot R\right) \cdot \frac{\bar{s}}{2} \tag{15}$$

$$t_C = t_i \frac{A_C}{\pi \frac{R^2 - r^2}{2}} \tag{16}$$

In equation (16), R and r are the average outer and inner radius of the section of the ring undergoing the deformation, respectively.

In order to properly calculate the heat exchange area, it should be noted that both thickness and height of the ring vary according to parabolic laws [8] and, for this reason, the distributions of height, thickness, external radius and internal radius are not uniform. If linear variations were applied, it would result in a rough approximation. A better estimation for these geometrical data can be obtained by adopting a parabolic variation between the beginning and the end of the considered slice, assuring the continuity of the first derivative at the transition between slices. The values of $R_{med,par}$ and $r_{med,par}$ used in Eq. (17) are calculated considering the values of outer, and inner, radius of two consecutive slices. They are then considered as the average value for the outer and inner radius for the half ring which exited the mandrel-main roll gap and is entering the axial rolls gap.

$$A_{equiv,C} = 2\left[\frac{\pi}{2}\cdot\left(R_{med,par}{}^{2} - r_{med,par}{}^{2}\right)\right] \tag{17}$$

In Eq. (17), the top area, or bottom, area of half ring is calculated and multiplied by 2 in order to take into account that both upper and lower axial roll are in contact with the ring.

The conductive heat exchange equation assumes the formulation of (18) where the values of t_C and $A_{equiv,C}$ are calculated using (16) and (17) respectively, and where half of the volume of the ring is considered, since only the half part of the ring exited from mandrel-main roll gap and entering the axial roll gap is considered. This subdivision allows calculating the average temperature for the ring at each half round of the process.

$$T_{axial,i} = \left(T_{j-1} - T_T\right)\cdot\exp\left(\frac{2A_{equiv,C}\cdot t_C\cdot HTC}{C\rho V}\right) \tag{18}$$

The definition of T_T, C, ρ, HTC and V is the same as detailed below equation (8).

If the ring is considered to rotate clockwise, the value of T_{j-1} will be the temperature resulting from the application of the mixed convective-radiant heat exchange model (detailed below) to the half of the ring between the mandrel-main roll gap and the axial rolls gap. $T_{axial,i}$ is then the average temperature of the ring, for i-round, after contact in the axial rolls deformation gap.

2.3 Convective-radiant heat exchange model

Convective and radiant heat exchange are phenomena related to the interaction of a hot body with the environment and they differ from the conductive heat exchange, where the phenomenon depends on contact between ring and tools. The convective part can be expressed by Newton's convective law, Eq. (19), whereas the radiant part by the radiation law, Eq. (20). Both phenomena are considered to act continuously during the rotation of the ring when the deformed slice moves from one deformation gap to the following one.

The adopted lumped model approximates this continuous heat exchange: the ring is considered to exit the mandrel-main roll gap with a temperature dependent on the conductive term and will cool down for half of the round time, on half of its surface, due to convective and radiant heat loss. The same reasoning is adopted after the axial rolls gap, where the same convective-radiant heat exchange model

is applied considering, as starting temperature, that resulting one from the conductive heat exchange in the axial rolls gap.

Assuming a constant convective heat transfer coefficient during the whole process, and calculating an equivalent heat transfer coefficient that includes both convective and radiant heat losses, Eq. (21), the temperature variation can be calculated as in (22). T_{amb} is the environment temperature (considered as a constant), $T_{i,k}$ is the temperature calculated in the previous stage (mandrel-main roll or axial rolls, see Fig. 1) for the i-round, and t_i is the time required to complete the generic i-round of the process.

$$\left.\frac{dQ}{dt}\right|_{conv} = A \cdot HTC\left(T - T_{amb}\right) \tag{19}$$

$$\left.\frac{dQ}{dt}\right|_{rad} = \varepsilon \cdot \sigma \cdot A \cdot \left(T^4 - {T_{amb}}^4\right) \tag{20}$$

$$HTC_{equiv} = HTC_{conv} + \varepsilon\sigma \cdot \left(T_{i,k} + T_{amb}\right)\left({T_{i,k}}^2 + {T_{amb}}^2\right) \tag{21}$$

$$T_{i,C-R} = T_{amb} + \left(T_{i,k} - T_{amb}\right)\exp\left[\left(-\frac{A \cdot HTC_{equiv}}{C\rho V}\right)t_i\right] \tag{22}$$

The definition of T_T, C, ρ and V is the same as detailed below equation (8). HTC_{conv} is the heat transfer coefficient for the convective heat exchange, σ is the Stefan-Boltzmann constant equal to 5.670373 W/m^{2}K^4 and ε the radiation coefficient (emissivity) of the material of the ring. The volume is considered as a constant value along the process thanks to volume constancy principle in plastic deformation.

3. Model for the prediction of the forming forces in the mandrel-main roll deformation gap

If the ring has a sufficiently large radius compared to the projection of the contact arc between the tools and the ring, the application of the slip-line solution developed by Hill for flat indenters, illustrated in Fig.5a, gives reasonable results in terms of the prediction of the radial forming force. However, as it will be shown in the results section, if the external diameter is sufficiently small, the curvature of the ring is no longer negligible and the direct application of the Hill's solution results in an underestimation of the radial forming force. Moreover, also the average mandrel feeding speed during the process has been shown to influence the quality of the prediction of the radial forming force. These effects are further investigated and the results are presented in sections 5 and 6 below where different configurations of the ring and different setups have been tested.

The slip-line solution derived by Hill for flat indenters [10] has been developed for the case of a flat punch acting on a flat surface where the stress field is considered symmetric with respect to the axis of the punch and degenerates into a single point after a certain depth h, as shown in Fig. 5a. This degeneration point "**F**" of the stress field is assumed to be in the middle of the ring section, a condition that also ensures to have plastic deformation along the whole thickness, resulting in the expansion of the ring.

In the RARR process, the contact zone (Fig. 5b), can be approximated as a flat surface if two initial assumptions are fulfilled. These are that the real shape of the entire ring is not taken into account (but only the contact zone in the mandrel-main roll deformation gap is considered) and that the ratio

between the projection of the contact arc and ring diameter (inner and outer) is sufficiently large. In this case, the application of the flat indenters slip-line solution results in a good representation of reality. However, if the diameter of the ring is small the curvature is no longer negligible and the approximation of the contact as a flat surface results in an underestimation of the process forces, as it will be proved later.

Moreover, as previously pointed out, the contact length between tools and ring used for the calculation of either heat exchange area or process forces is assumed to have a common value for both mandrel and main roll side, represented by the projection of the contact arc onto the x-axis as shown in Fig. 2. For this reason, the radial forming force is considered to have the same value either it is calculated from the main roll side or from the mandrel side.

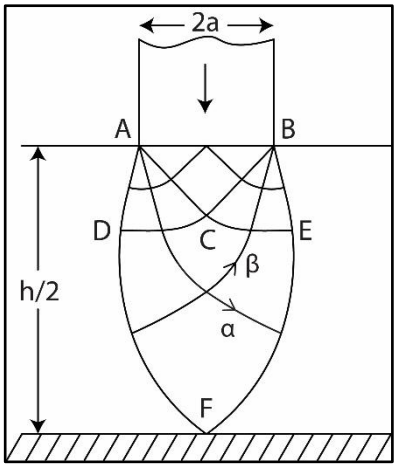

Figure 5a - Hill's slip-line solution for flat indenter [10]

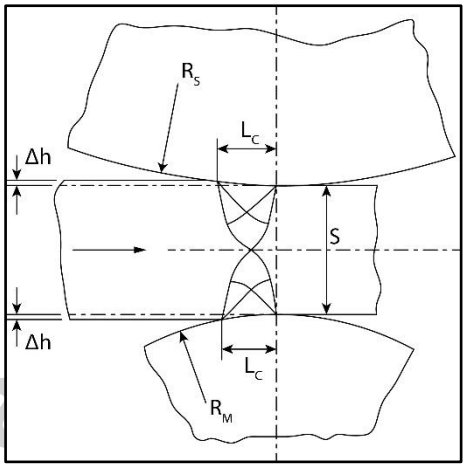

Figure 5b - Hawkyard's [6] application of the Hill's solution to the ring rolling process

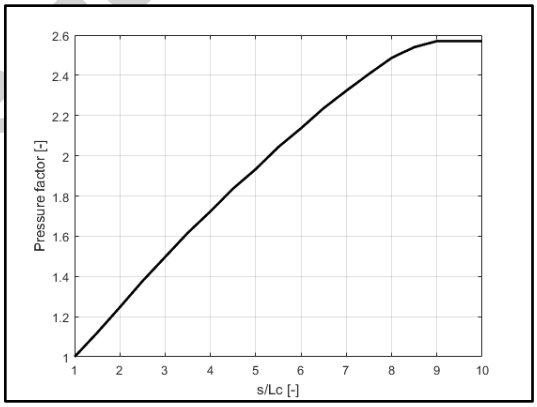

Figure 6 – Pressure factor for the slip-line solution for flat indenters [10]

The solution of the slip-line field for flat indenters is given in [6] in terms of chart for the pressure factor variation according to the ratio s / L_C, Fig. 6, representing the ratio between thickness of the ring at the exit of the deformation gap and the projection of the contact arc.

However, to allow a faster and more precise calculation of the solution of the slip-line field, the pressure factor chart, Fig. 6, has been converted into the parabolic equation (23) and used to determine the value

of γ to be used in the force equation (24). In (24), k stands for the yield shear strength of the material whereas $\bar{h}$ is the average height of the slice entering the roll gap. Referring to the discretization of the ring into slices [8], the value of the pressure factor γ has been calculated for each slice and for each round of the process required to obtain the final shape of the ring.

$$\gamma = -0.0098\left(\frac{s}{L_C}\right)^2 + 0.2999\left(\frac{s}{L_C}\right) + 0.6909 \tag{23}$$

$$F = 2k\gamma\bar{h}L_C \tag{24}$$

Concerning the deformation mode, the Hill's slip-line solution [10] utilized in this paper has been developed under the plane strain hypothesis then both the plastic flow at the onset and at the exit of the deformation gap are considered to be oriented along the direction orthogonal to the line joining the mandrel and main roll centers. The slip-line solution under the plane strain hypothesis is not so far from most of the considered cases, where the third strain in both the deformation gaps is usually quite low if compared with the other two strains, as confirmed by FE simulation. According to this hypothesis, the assumption of a plane strain field is reasonable for each one of the deformations occurring in a single rotation of the ring, but these strain fields present different orientations in the space:

- In the mandrel-main roll gap, the deformation is applied in the radial direction and, consequently, a circumferential strain arises to keep the volume constancy. The strain along the vertical direction is considered as negligible;
- In the axial rolls gap, the deformation is applied in the vertical direction and, consequently, a circumferential strain arises to keep the volume constancy. The strain along the radial direction is considered as negligible;

Therefore, the overall strain field is a 3D strain tensor, but if the deformation gaps are considered one by one, the application of a plane strain hypothesis in not so far from the reality. The mathematical model developed by the authors in previous work [9], which is able to calculate all the three principal strain components of the strain tensor, is therefore adopted for the calculation of the effective strain and strain rate, used for the calculation of flow stress of the material.

4. Model validation

Using the model for the calculation of strain and strain rate [9] and temperature as described in the previous section, the flow stress of the material can be calculated for each slice of the ring from the beginning to the end of the deformation, allowing us to map its evolution throughout the process. Afterwards, Eq. (24) can be used to calculate the radial forming force in the mandrel-main roll deformation gap, where the required geometrical parameters can be calculated utilizing the algorithm proposed in a previous work of the authors [8].

In order to validate both the model for the prediction of the temperature and the reliability of the application of the previously mentioned Hill's solution to the RARR process, the case study presented in the work of Kim et al. [14] was considered. The flow stress equation for the material used in [14], stainless steel alloy AISI-304, is given by (25) and the relevant model constants are listed in Table 1. The relevant data for the ring, the ring rolling mill, the process parameters and additional AISI-304 material properties are summarized in Table 2.

$$\sigma = K_0 \left(a_0 + a_1 \varepsilon\right)^n \left(b_0 + b_1 \dot{\varepsilon}\right)^m \tag{25}$$

Table 1 – AISI-304 material model constants [14]

Temperature [°C]	K_0	a_0	a_1	n	b_0	b_1	m
1100	160.00	0.00	2.14	0.09	0.00	0.10	0.10
1000	225.20	0.00	0.04	0.09	0.17	1.30	0.13
800	330.90	0.00	0.17	0.08	4.50	3.20	0.06

Table 2 – Model validation case study data [14]

Parameters	**Value**
Ring blank outer diameter [mm]	454
Ring blank inner diameter [mm]	150
Ring blank height [mm]	200
Final ring outer diameter [mm]	900
Final ring inner diameter [mm]	722
Final ring height [mm]	110
Radius of the main roll [mm]	423
Radius of the mandrel [mm]	65
Length of the axial rolls [mm]	800
Half of cone vertex angle [°]	20
Main roll rotational speed [rad/s]	2
Mandrel initial feeding speed [mm/s]	5
Mandrel final feeding speed [mm/s]	1
Friction coefficient	0.5
Temperature of the environment [°C]	20
Tool temperature [°C]	150
Ring initial temperature [°C]	1100
*Density [kg/m^3]	7770
**Specific heat capacity [J/kgK]	610
**Emissivity [-]	0.25
**Heat transfer coefficient (conduction) [W/m^{2}K]	20000
**Heat transfer coefficient (convection) [W/m^{2}K]	50

In Table 2, the parameters which has a "*" before the description have been taken from the reference of [14], where the material model (25) was also derived from. Differently, the parameters with "**", have been set-up by authors based on the MATILDA® (Material Information Link and Database Service) archive for the AISI-304 steel.

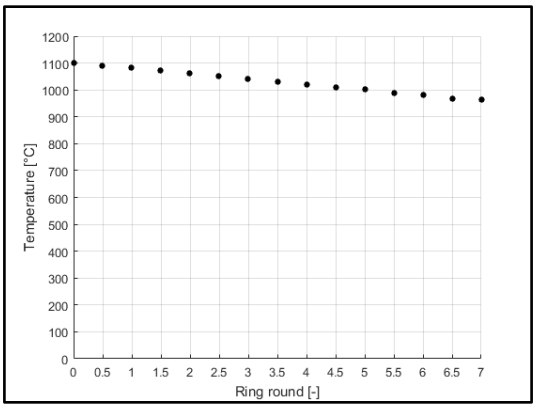

Figure 7.a - Analytical prediction of the temperature evolution for the case study [14]

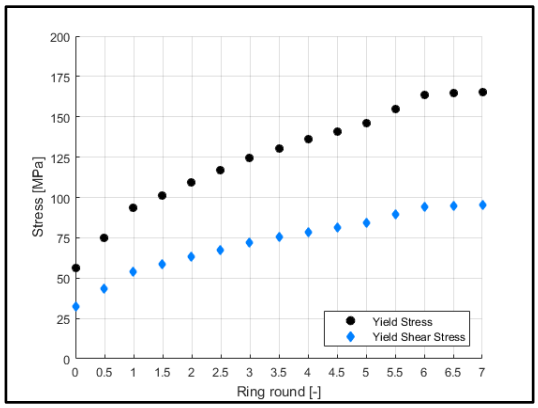

Figure 7.b - Analytical prediction of the flow stress for the case study [14]

In [14], the Mongonon and Thomas [15] method has been utilized for the determination of the flow stress of the material based on the martensite fraction in the steel alloy. Based on this calculation, and utilizing the inverse calibration method, the constants for the material model shown in Eq. (25) have been calculated for the temperature range of interested in the specific process condition of this study case.

Since the mathematical model for the calculation of the temperature evolution in the ring has been developed under a lumped hypothesis, the result in Fig. 7a represents the average temperature for the whole ring at the end of each half round of the process. Considering the temperature evolution in Fig. 7a, in addition to the rules defined in [9] for the determination of strain and strain rate, the increment of the yield stress has been calculated using (25), Fig. 7b, converted into yield shear stress utilizing the von Mises criterion and used in (24) to determine the radial forming force required in the process. Authors' analytical prediction is compared, in Fig. 8, with the experimental and FE simulation results from [14].

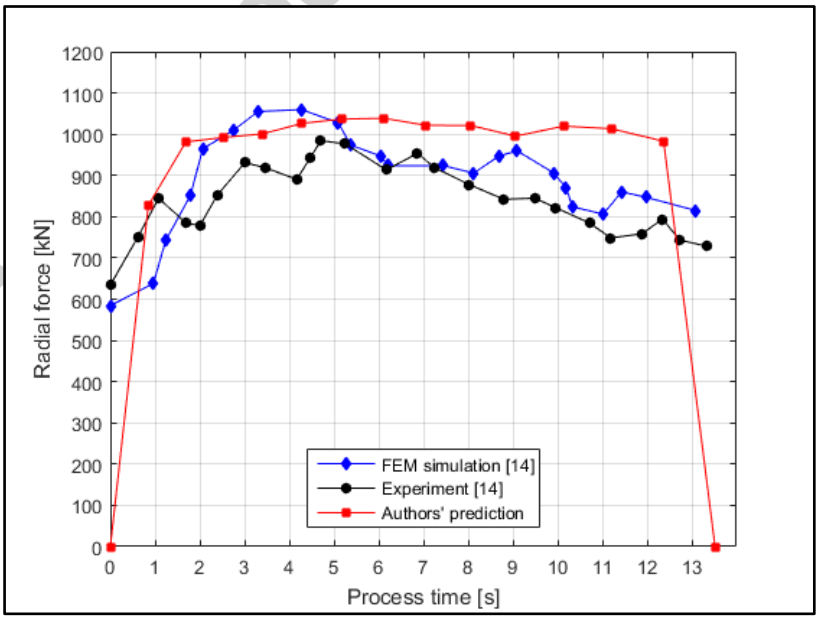

Figure 8 - Radial forming force comparison for the case study [14]

Although some differences are evident among analytical, experimental and FE results, as shown in Fig. 8, mainly in the final stages of the process, the maximum value calculated utilizing authors' prediction models is 1038.7 kN (Authors' prediction curve) whereas the maximum value calculated by FE simulation [14] is 1059.6 kN, and by experiment [14] is 984.4 kN. The relative errors are 2.0% and 5.5% respectively. As pointed out at the beginning of the paper, the main aim of the present research work is the development of an algorithm able to calculate the maximum radial forming force in the RARR process then, to this end, the results obtained by the cross-comparisons among the analytical model, literature FE simulation and experiment have confirmed the reliability of the proposed approach.

Based on the successful validation performed using previous literature studies, the proposed and previously developed analytical models [8, 9], have been applied to a variety of different case studies; the design of experiments of the FEM simulation is presented in the following paragraph.

5. Model implementation

In the analyzed case studies, the values for geometry, strain and strain rate (calculated utilizing authors' models [8] and [9]) were used, together with the temperature prediction model, to calculate the flow stress of the material by utilizing Eq. (26), where ε is the strain, $\dot{\varepsilon}$ the strain rate and T the temperature of considered slice of the ring at the specified round of the process. The radial forming force was then determined using Eq. (24). In the following case studies, the steel alloy 42CrMo4 was used. FEM simulations and analytical calculations have been carried out using the same flow stress equation (26), whose constants are summarized in Table 3. Additional information related to the 42CrMo4 steel alloy are given in Fig. 9.a, 9.b and 9.c and in Table 4. The value of yield stress derived using (26) has been divided by $\sqrt{3}$, according to von Mises yield criterion, in order to obtain the yield shear stress in plane strain conditions, required in (24) for the determination of the radial forming force.

$$\sigma = C_1 e^{(C_2 \cdot T)} \varepsilon^{(n_1 \cdot T + n_2)} e^{\left(\frac{L_1 \cdot T + L_2}{\varepsilon}\right)} \dot{\varepsilon}^{(m_1 \cdot T + m_2)} \tag{26}$$

Table 3 - 42CrMo4 alloy material model ranges and constants

Parameters	**Value**
Temperature range for the model [°C]	800–1250
Strain range for the model [–]	0.05–2
Strain rate range for the model [1/s]	0.01–150
C_1	5290.47
C_2	–0.0036967
n_1	–0.000334025
n_2	0.20612
L_1	–8.26584e-5
L_2	0.0289085
m_1	0.000300752
m_2	–0.156181

Table 4 - Ring rolling mill characteristics and process/material parameters

Parameters	**Value**

Radius of the main roll [mm]	325
Radius of the mandrel [mm]	125
Length of the axial rolls [mm]	595.9
Half of cone vertex angle [°]	17.5
Main roll rotational speed [rad/s]	3.0
Friction coefficient	0.3
Temperature of the environment [°C]	50
Ring initial temperature [°C]	1200
Tool temperature [°C]	150
Density [kg/m^3]	7847
Specific heat capacity [J/kgK]	According to Fig. 9c
Emissivity [-]	0.25
Heat transfer coefficient (conduction) [W/m^{2}K]	20000
Heat transfer coefficient (convection) [W/m^{2}K]	50

The material Eq. (26), implemented in Simufact.Forming 12.03, is the GMT-MATILDA® material equation, is derived from the well-known Hansel-Spittel model [16]; the material model constants and properties for the 42CrMo4 steel alloy, derived from the MATILDA® (Material Information Link and Database Service) archive, are available in the material database of Simufact.Forming 12.03, the FEM software used for the simulations. The same equation, along with the same model constants and properties, have been utilized both in the FEM simulations and in the analytical calculations, in order to test the proposed approach under the same conditions.

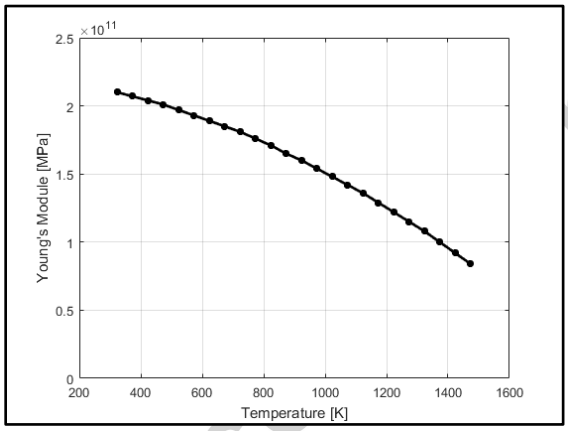

Figure 9.a - Young's modulus of 42CrMo4 steel

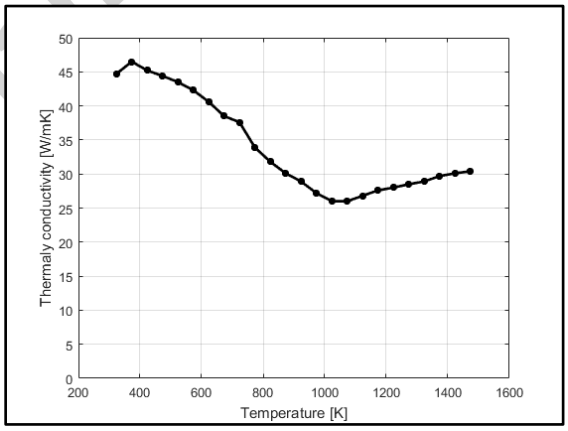

Figure 9.b - Thermal conductivity of 42CrMo4 steel

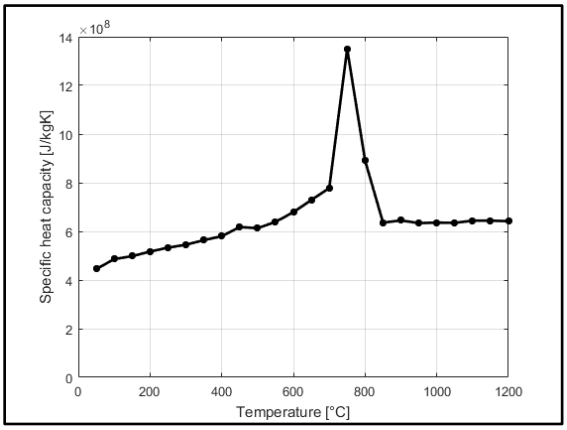

Figure 9.c - Specific heat capacity of 42CrMo4 steel

For the FEM simulations, the software Simufact.Forming 12.03 was used. A full thermo-mechanical explicit FE analysis, considering rigid dies with heat exchange has been performed for all the study cases. The utilized solver for the simulation is the MUltifrontal Massively Parallel sparse direct Solver (MUMPS), especially indicated for solving systems of linear equations of the form A*x = b, where A is a square sparse matrix that can be either asymmetric, symmetric positive definite, or general symmetric. MUMPS implements a direct method based on a multifrontal approach, which performs a Gaussian factorization.

The kinematics of deformation is formulated according to the updated Lagrangian algorithm where the reference configuration is set at the incremental motion n+1. True (or Cauchy) stress and an energetically conjugate strain measure, namely the true strain, are used in the constitutive relationship. The updated Lagrangian approach is particularly indicated in case of large deformation, so it fits the ring rolling process. FE models were based on 3D arbitrarily distorted brick, an hexahedral eight-node, isoparametric, arbitrary element (Marc element type 7) associated with three-dimensional eight-node brick (heat transfer element) an eight-node, isoparametric, arbitrary hexahedral element written for three-dimensional heat transfer applications (Marc element type 43).

During the contact process, a contact tolerance is associated with each surface. If a node is within the contact tolerance, it is considered to be in contact with the segment. The contact tolerance is determined as 1/20 of the smallest element size of all elements in any contact body. For a continuum element, the element size is defined as the smallest edge of the surrounding box (3D), set up in the global coordinate system and a node separates from a body when the stress exceeds 20 MPa. Contact affects the friction and in order to overcome the discontinuity of friction when relative velocity is zero, a nonlinear arctangent smoothing function, based on the relative sliding velocity between contact bodies, was defined adopting a threshold of 0.001 mm/s for the relative velocity below which sticking is simulated. Concerning the convergence criteria, the control is performed on two different levels: i) the maximum allowed residual convergence ratio between two consecutive steps, for the nodal displacement calculation, is set to 0.25 whereas ii) it is set to 0.35 for the nodal force.

In order to avoid any alteration of the results due to mesh size, a mesh size-influence analysis has been conducted on Case 1. Since the final target of this research work is the accurate estimation of the radial forming force, four different simulation with four different level of mesh have been run considering Case 1 settings (Table 6), comparing the results in term of maximum radial forming force.

Table 5 – Mesh influence analysis (Case 1)

	Mesh size [mm]						
Mesh case	**Axial**	**Radial**	**Tangential**	**Number of elements**	**Computational time [h-m]**	**Max radial force [kN]**	**Relative error**
0	34	32	34	1728	5h 38’	1290.2	-
1	24	22	24	4560	10h 32’	1395.1	7.52 %
2	20	18	20	8640	16h 25’	1379.8	1.11 %
3	14	12	14	20280	73h 3’	1366.7	0.96 %

As shown in Table 5, the relative difference between mesh case 0 and 1 is too much high, the mesh case 2 has been also run, showing an error a little greater than 1%. To confirm the trend, also mesh case 3 was run, with a considerable increase of the computational time. For this reason, being the computation time of mesh case 2 lower than mesh case 3 and being the result, in terms of maximum radial forming force, very similar each other, the mesh settings of mesh case 2 have been utilized in all the analyzed

study cases. For this reason, all FE models were meshed utilizing a hexahedral 3D element with dimensions of 20 mm (axial), 18 mm (radial) and 20 mm (tangential).

The analysis were conducted on rings having final outer diameters from 650 mm to 2400 mm. Each group of rings having the same final outer diameter will be subsequently called a "ring family". For each ring family, three different ratios of final height to thickness, subsequently called G_f (geometry factor), have been tested. These ranged from $G_f = 3$ (slim rectangular ring section) to $G_f = 1$ (square ring section). The data for the ring rolling mill and the process conditions set-up in the simulations are listed in Table 4. The geometrical data for the ring blank, final ring and mandrel feeding speeds (initial and final) for all the case studies are summarized in Table 6.

In order to understand the influence of G_f and of the dimensions of the ring, especially in terms of its final outer diameter, on the quality of the prediction of the radial forming force, the value of the initial and final feeding speed for the mandrel have been initially kept as constant as possible, but always within the feasible ranges defined in [8]. For each of the comparisons performed in the present study, the quality of the prediction of the radial forming force has been measured and is expressed in terms of the ratio between the result of the analytical estimation and the result of the relevant FEM simulation. This ratio is represented by the symbol ξ.

Table 6 - Simulation settings

		Ring blank dimensions			Final ring dimensions			Mandrel feeding speed	
Ring Case	G_f	**Outer diameter [mm]**	**Inner diameter [mm]**	**Height [mm]**	**Outer diameter [mm]**	**Inner diameter [mm]**	**Height [mm]**	**Initial speed [mm/s]**	**Final speed [mm/s]**
1	3.0	575.25	325.00	218.75	1100.00	975.00	190.00	7.2	5.0
2	2.0	621.60	325.00	209.00	1100.00	930.00	170.00	6.5	4.5
3	1.0	668.70	325.00	171.80	1100.00	855.00	122.50	5.8	4.5
4	3.0	518.85	325.00	195.43	800.00	680.00	180.00	7.7	6.6
5	2.0	550.92	325.00	175.44	800.00	645.00	155.00	7.5	5.0
6	1.0	574.51	325.00	124.76	800.00	600.00	100.00	6.0	4.5
7	3.0	821.74	600.00	214.69	1400.00	1270.00	195.00	6.0	3.9
8	2.0	876.15	600.00	208.24	1400.00	1220.00	180.00	5.5	3.5
9	1.0	917.87	600.00	158.93	1400.00	1130.00	135.00	4.5	3.0
10	3.0	544.04	325.00	201.98	950.00	830.00	180.00	6.7	4.6
11	2.0	589.95	325.00	194.85	950.00	785.00	165.00	6.0	4.5
12	1.0	650.19	325.00	162.60	950.00	700.00	125.00	6.0	4.5
13	3.0	837.80	600.00	207.21	1700.00	1580.00	180.00	6.0	3.0
14	2.0	897.70	600.00	209.36	1700.00	1530.00	170.00	5.5	3.0
15	1.0	943.41	600.00	171.71	1700.00	1460.00	120.00	4.7	3.0
16	3.0	490.53	325.00	188.81	650.00	530.00	180.00	7.0	5.0
17	2.0	510.93	325.00	156.24	650.00	505.00	145.00	7.0	5.0
18	1.0	549.33	325.00	112.17	650.00	450.00	100.00	6.0	4.5
19	3.0	682.81	450.00	213.88	1250.00	1125.00	190.00	6.5	4.0

20	2.0	730.52	450.00	203.34	1250.00	1080.00	170.00	6.5	4.0
21	1.0	809.30	450.00	179.65	1250.00	980.00	135.00	5.7	4.0
22	3.0	875.65	600.00	226.25	2000.00	1875.00	190.00	5.5	2.7
23	2.0	944.45	600.00	232.41	2000.00	1820.00	180.00	5.5	2.7
24	1.0	1049.33	600.00	224.67	2000.00	1700.00	150.00	4.7	2.7
25	3.0	908.68	600.00	243.72	2200.00	2067.00	200.00	5.5	2.3
26	2.0	947.15	600.00	227.61	2200.00	2030.00	170.00	5.3	2.3
27	1.0	1070.05	600.00	235.03	2200.00	1900.00	150.00	4.5	2.3
28	3.0	910.07	600.00	237.13	2400.00	2275.00	190.00	5.5	2.3
29	2.0	964.80	600.00	234.40	2400.00	2230.00	170.00	5.3	2.3
30	1.0	1089.59	600.00	244.79	2400.00	2100.00	150.00	4.4	2.3

6. Results and discussion

Table 7 gives the results of prediction of the temperature during the process, obtained utilizing the models proposed in section 2, together with the relevant relative percentage error. Since two different values for the surface temperature of the ring were available in the FEM simulations, one for the inner radius and one for the outer one, the relative error is taken as the error between the average of these two values and the one calculated using the analytical approach described in section 2.

Table 7 – Temperature results comparison

		Round of the process [-]						
Ring Case	**Value**	**1**	**2**	**3**	**4**	**5**	**6**	**7**
1	FE Simulation	1182.9	1159.8	1136.0	1111.1	1084.0	1068.5	
	Analytical	1179.0	1143.5	1119.5	1094.0	1075.5	1065.0	
	% Error	0.33	1.43	1.48	1.56	0.79	0.33	
2	FE Simulation	1184.3	1161.7	1138.4	1114.3	1088.3	1065.9	
	Analytical	1182.0	1143.5	1110.5	1089.0	1072.0	1064.0	
	% Error	0.20	1.59	2.52	2.33	1.52	0.18	
3	FE Simulation	1186.0	1162.2	1137.5	1111.6	1087.7		
	Analytical	1184.0	1152.0	1173.5	1098.0	1079.0		
	% Error	0.17	0.89	-3.06	1.23	0.80		
4	FE Simulation	1179.1	1151.2	1121.7	1107.9	1107.9		
	Analytical	1186.0	1146.0	1115.5	1091.0	1074.5		
	% Error	-0.59	0.46	0.56	1.56	3.12		
5	FE Simulation	1181.0	1154.2	1126.5	1113.7			
	Analytical	1183.5	1148.5	1114.0	1090.5			
	% Error	-0.21	0.49	1.12	2.13			
6	FE Simulation	1183.5	1154.4	1127.1	1127.1			
	Analytical	1181.5	1149.0	1108.5	1086.5			
	% Error	0.17	0.47	1.68	3.74			

7	FE Simulation	1181.4	1153.1	1122.1	1096.3			
	Analytical	1182.0	1141.5	1123.0	1106.0			
	% Error	-0.05	1.02	-0.08	-0.88			
8	FE Simulation	1184.4	1158.9	1131.7	1104.2			
	Analytical	1183.0	1152.5	1130.0	1111.5			
	% Error	0.12	0.56	0.15	-0.66			
9	FE Simulation	1186.2	1157.9	1127.0	1115.0			
	Analytical	1179.5	1146.5	1122.0	1108.0			
	% Error	0.57	1.00	0.45	0.63			
10	FE Simulation	1181.5	1156.5	1130.6	1103.2	1073.2		
	Analytical	1180.5	1140.5	1098.0	1069.5	1051.5		
	% Error	0.09	1.41	2.97	3.15	2.06		
11	FE Simulation	1179.2	1156.0	1131.8	1106.5	1079.1		
	Analytical	1180.0	1142.5	1110.0	1083.5	1066.5		
	% Error	-0.07	1.18	1.97	2.13	1.18		
12	FE Simulation	1185.5	1160.8	1135.2	1112.9			
	Analytical	1185.0	1151.5	1119.0	1097.5			
	% Error	0.04	0.81	1.45	1.40			
13	FE Simulation	1182.2	1154.3	1124.0	1090.3	1059.7		
	Analytical	1182.0	1145.5	1128.0	1110.0	1096.0		
	% Error	0.02	0.77	-0.36	-1.77	-3.31		
14	FE Simulation	1185.1	1160.1	1133.4	1104.4	1071.7	1060.9	
	Analytical	1179.0	1142.5	1120.5	1109.5	1099.5	1094.0	
	% Error	0.52	1.54	1.15	-0.46	-2.53	-3.03	
15	FE Simulation	1186.5	1159.4	1129.8	1097.2	1067.4		
	Analytical	1182.0	1152.5	1128.5	1107.0	1094.5		
	% Error	0.38	0.60	0.12	-0.89	-2.47		

16	FE Simulation	1178.1	1150.1	1129.5	1108.0			
	Analytical	1157.0	1108.5	1092.5	1094.5			
	% Error	1.83	3.75	3.38	1.23			
17	FE Simulation	1179.6	1151.0	1122.5				
	Analytical	1134.0	1098.0	1092.5				
	% Error	4.02	4.83	2.74				
18	FE Simulation	1182.9	1165.8					
	Analytical	1163.5	1117.5					
	% Error	1.67	4.32					
19	FE Simulation	1182.1	1156.2	1128.7	1098.8	1073.7		
	Analytical	1192.0	1157.0	1135.5	1114.5	1104.0		
	% Error	-0.83	-0.07	-0.60	-1.41	-2.74		
20	FE Simulation	1184.0	1158.9	1132.5	1104.3	1072.1		
	Analytical	1188.0	1156.5	1135.0	1114.0	1098.5		
	% Error	-0.34	0.21	-0.22	-0.87	-2.40		
21	FE Simulation	1185.0	1158.0	1140.0	1122.0			
	Analytical	1185.5	1155.5	1131.0	1109.5			
	% Error	-0.04	0.22	0.80	1.13			
22	FE Simulation	1184.4	1157.9	1129.5	1098.7	1063.7	1042.9	
	Analytical	1185.0	1152.5	1129.0	1110.5	1099.0	1089.5	
	% Error	-0.05	0.47	0.05	-1.07	-3.22	-4.28	

23	FE Simulation	1186.9	1163.0	1137.9	1111	1081.1	1063.8	
	Analytical	1185.5	1149.5	1121.0	1101.0	1085.0	1078.0	
	% Error	0.12	1.18	1.50	0.91	-0.36	-1.32	
24	FE Simulation	1189.0	1165.7	1141.1	1114.9	1085.4	1068.3	
	Analytical	1186.0	1153.5	1126.5	1105.5	1096.5	1089.5	
	% Error	0.25	1.06	1.29	0.85	-1.02	-1.95	
25	FE Simulation	1185.5	1160.8	1134.7	1106.6	1075.3	1056.9	
	Analytical	1184.0	1148.0	1122.5	1108.0	1097.5	1090.5	
	% Error	0.12	1.12	1.09	-0.12	-2.02	-3.08	
26	FE Simulation	1186.6	1161.9	1135.8	1107.8	1076.4	1058.1	
	Analytical	1184.5	1157.5	1134.0	1117.5	1103.5	1093.5	
	% Error	0.18	0.38	0.16	-0.87	-2.46	-3.24	
27	FE Simulation	1189.5	1167.3	1144.0	1119.5	1092.2	1076.5	1028.1
	Analytical	1187.5	1164.0	1137.0	1116.5	1102.5	1090.5	1084.0
	% Error	0.17	0.28	0.62	0.27	-0.93	-1.28	-5.15
28	FE Simulation	1185.5	1159.1	1131.1	1100.9	1066.8	1046.7	
	Analytical	1179.0	1146.5	1119.0	1101.0	1088.0	1080.5	
	% Error	0.55	1.10	1.08	-0.01	-1.95	-3.12	
29	FE Simulation	1187.3	1163.8	1138.9	1112.4	1082.9	1065.7	1008.8
	Analytical	1183.0	1151.0	1122.0	1101.5	1091.0	1083.5	1076.5
	% Error	0.37	1.11	1.51	0.99	-0.75	-1.65	-6.29
30	FE Simulation	1189,8	1168,4	1146,0	1122,4	1096,2	1081,1	1027,6
	Analytical	1173,5	1155,0	1131,5	1112,5	1099,0	1092,0	1086,0
	% Error	1,39	1,16	1,28	0,89	-0,25	-0,99	-5,38

The prediction of the temperature in the ring has shown to be in good agreement with the result of the relevant FEM simulation; among all the 30 analyzed case study cases the maximum error is 6.97% whereas the average error is 1.87%, showing the reliability of the proposed approach for the estimation of the temperature in the ring during the process. Although the model calculates the value of the average temperature of the ring for each half round, reporting also the half round-based predictions would have been too tedious, hence only the round-based predictions are reported in the paper (in Table 7), whereas the half round-based prediction are accessible on request to the corresponding author.

Concerning the calculation of radial forming force, the parameters most affecting the analytical force prediction have been identified in the shape factor G_f and the final outer diameter of the ring D_f. As shown in Fig. 10, for small values of the ring final outer diameter, the error can reach 28%. This underestimation is a consequence of the initial hypothesis of approximating the contact between ring and tools as a straight line, which has shown to be reasonable for relatively large rings (D_f > 1100) but not for relatively small rings (D_f < 1100).

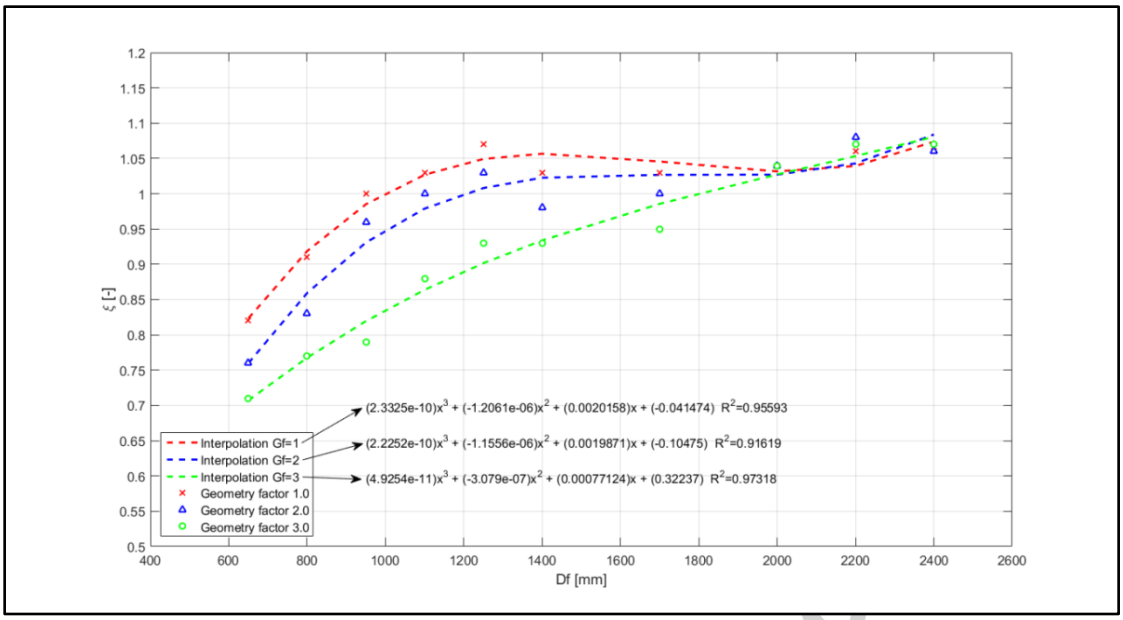

Figure 10 – Accuracy of the radial force prediction versus D_F (for different G_f)

Moreover, for most of the ring families, it is observed that the variation of the shape factor G_f implies a variation of ξ, even within the same ring family (Fig. 10). This effect tends to disappear for large rings with a final diameter ≥ 2000 mm. For these large rings, the analytical prediction seems to be almost independent of shape factor and slightly overestimated (between +4% and +7%) with respect to the relevant FEM simulation results. Even so, for rings having final diameters between 1100 mm (except the ring with D_f = 1100 mm and G_f = 3 for which ξ = 0.88) and 2400 mm, the errors are limited to ±10%. Thus, the developed algorithm, together with authors' previous ones [8, 9], along with the Hill's slip line flat indenters solution, allows a real time estimation of the maximum radial forming force with a limited error. Instead, if the FE approach is used, the computational time for the calculation can range between 10 hours and 28 hours (for the analyzed case studies on a i7-processor computer adopting parallel computing). This fast approach allows the exploration of many process parameter combinations in a relatively short time, enhancing the potentiality of the design stage. Moreover, based on the results of this study, if the proposed approach is applied on rings having the D_f < 1100 mm, suitable correction can be adopted to limit the error and make the prediction to be reliable also in these cases. Additional comments about how to operate in case D_f < 1100 mm are reported in the end of this paragraph. In addition, in order to analyze the influence of the variation of the mandrel feeding speed on the accuracy of the prediction of the radial forming force, the accuracy factor ξ has been plotted with respect to the average mandrel feeding speed, as shown in Fig. 11.

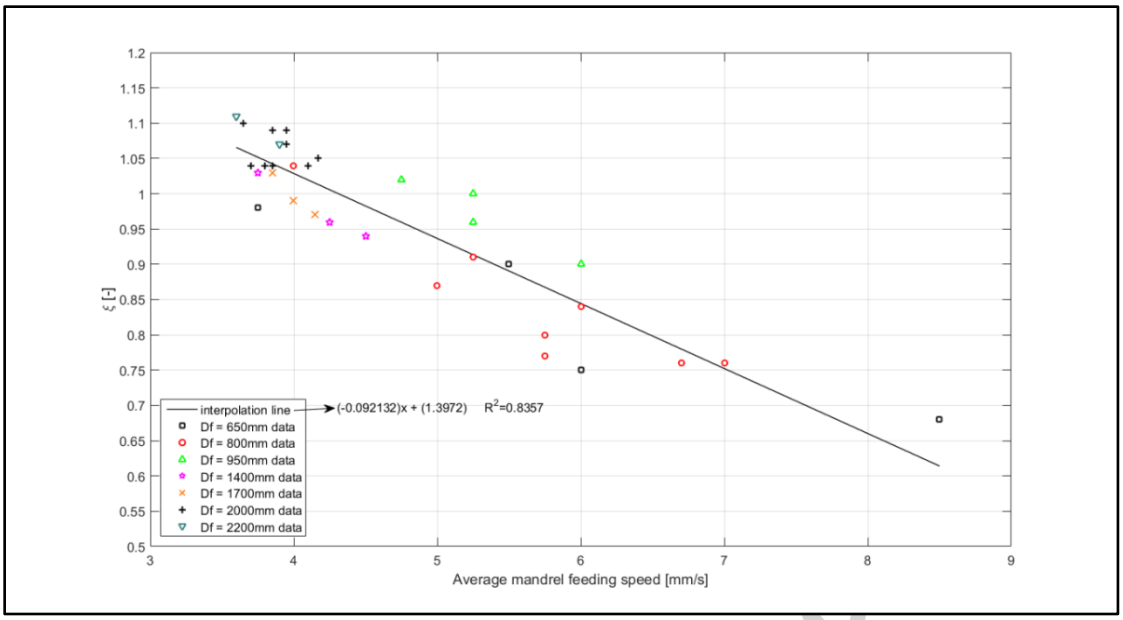

Figure 11 – Accuracy of the radial force prediction versus average mandrel feeding speed

Here, the average mandrel feeding speed is calculated as the average of the value at the beginning and at the end of the deformation process. In addition to the simulation cases shown in Table 6, additional FEM simulations, with the same geometrical parameters but different average values for the mandrel feeding speed, have been run in order to check the influence of the mandrel feeding speed; the comparison is shown in following Table 8, for Case 8 and Case 10. As previously done, also for these additional cases, the chosen values for initial and final mandrel feeding speed have been set within the ranges prescribed by [8].

As understandable from Fig. 11, and also from the results shown in Table 8, the higher the average mandrel feeding speed, the lower the quality factor ξ. In Table 8, case studies 8.1 and 10.1 share the same geometry and process settings as 8 and 10 in previous Table 6. Since the average mandrel feeding speed is the only parameter that varies, it is possible to conclude that there is a direct effect of the average mandrel feeding speed on the quality of the prediction of the radial forming force (ξ). This effect is summarized in Fig. 11, where all the results of the analyzed study cases have been gathered together and a linear correlation has been identified between the average mandrel feeding speed and the quality factor ξ.

Table 8 – Effect of the average mandrel feeding speed on ξ

Ring case	Initial mandrel feeding speed [mm/s]	Final mandrel feeding speed [mm/s]	Average mandrel feeding speed [mm/s]	ξ [-]
8	7.5	5.0	6.25	0.83
8.1	7.5	6.5	7.00	0.72
10	6.0	4.5	5.25	0.91

10.1	7.0	5.0	6.00	0.84

The proposed analysis has shown that both the ring final diameter and average mandrel feeding speed affect the quality factor ξ and this fact must be taken into account when the proposed prediction models are applied to rings having a final outer diameter lower than 1100 mm and where the average mandrel feeding speed is greater than 5 mm/s.

Finally, to analyze possible effects of the projection of the contact arc, Table 9 shows the data of the average projection of the contact arc between ring and tools for all the analyzed case studies (previously reported in Table 6). The values can be considered as almost constant among all the analyzed case studies, demonstrating how the contact arc alone does not give enough information to properly describe the interaction between ring and tools. With respect to the calculation of the projection of the contact arc, the mandrel and main roll radii are relevant variables, but their influence on the quality of the calculation of the radial forming force is out of the scope of the present research work.

Table 9 – Average contact arc projection for the case studies

Ring case	Contact arc value [mm]	Ring case	Contact arc value [mm]
1	34.18	**26**	30.27
3	34.45	**28**	29.25
5	34.37	**30**	30.32
6	33.17	**31**	34.18
8	32.83	**33**	35.20
10	31.46	**35**	35.40
11	35.34	**36**	34.90
13	34.36	**38**	35.42
15	32.20	**40**	35.05
16	32.08	**41**	35.87
18	32.34	**43**	36.04
20	33.92	**45**	35.57
21	35.22	**46**	36.25
23	35.31	**48**	35.98
25	33.72	**50**	35.98

In case the final outer diameter of the ring is lower than 1100 mm and if the average mandrel feeding speed is greater than 5 mm/s, in order to accurately estimated the radial forming force by utilizing the Hill's slip line solution, a correction factor proportional to the underestimation evidenced in Fig. (10) and (11) should be taken into account. For instance, for the study case 5 (final outer diameter 800 mm and final height/thickness ration 2.0), according to Fig. (10), the prediction of the radial forming force is affected by an underestimation of 17% compared with the relevant FE simulation. For this case, a correction factor equal to the underestimation should be adopted. In the same way, if the underestimation is caused by a high mandrel feeding speed, similar criteria should be adopted.

It should be anyway noted that, according to authors' previous work [8], the calculation of the feasible ranges for both initial and final mandrel feeding speed is not independent from the size of the ring itself. The forming limit condition that ensure plastic deformation along the whole thickness of the ring as well as avoid indentation of the ring surface make the range extreme values to become higher as the ring size decreases and vice-versa. This fact makes the results shown in Fig. (10) and (11) to be a different interpretation of the same limitation of the slip line solution for flat indenters when it is applied to ring rolling process. The analysis proposed in this paper details the limits in the utilization of this model and gives useful information about how to deal if this model is used outside these limits.

7. Conclusion

The wide analysis presented in this paper has shown that the proposed lumped parameters heat exchange model can predict the temperature evolution in a ring during the forming process with a maximum error of 7% and an average error of 1.8%, demonstrating the reliability of the proposed algorithm. The proposed heat exchange model was initially applied to an experimental case where laboratory data on forces, process parameters, geometry of the ring and material were available. The results of the comparison, in terms of ring geometry and forming force, encouraged the extension of the investigation to different ring geometries. For these investigations, different cross sections of the ring and different expansion rules have been used and the results of temperature and radial forming force have been successfully compared with the corresponding results of FEM simulations where i) the same material properties, ii) the same kinematics of the rolling mill, and iii) the same annular preform were adopted.

Regarding the prediction of the forming force, the application of the slip-line solution for flat indenters adapted to the ring rolling process, have shown acceptable results for most of the tested cases. Specifically, if the final external diameter of the ring is above 1100 mm and the average mandrel feeding speed is below 5 mm/s, the quality of the prediction is reasonably good with errors below 10%. If, instead, the final outer diameter of the ring is below 1100 mm the effect of ring curvature cannot be neglected and the flat indenter hypothesis does not adequately represent reality. In addition to that, when the average mandrel feeding speed is above 5 mm/s the model loses accuracy because of the linearization and simplifications adopted, especially regarding the velocity field. For these cases, the maximum error is limited to 28% and, at the preliminary stages of the design of ring rolling process, if an adequate safety factor is adopted, this error can be acceptable.

As regards the estimation of radial forming force, the model is able to take into account the effects of i) the ratio between final height and thickness of the ring, ii) the final outer diameter of the ring, iii) the mandrel feeding speed and iv) the material flow stress as function of strain, strain rate and temperature.

In conclusion, the proposed analytical models for the preliminary calculation of temperature evolution and required radial forming force, combined with previous authors' models for the prediction of ring geometry, strains and strain rate, give useful results for a wide range of industrially relevant cases, allowing the exploration of various combination of process parameters, checking their influence on important process variable (such as temperature and force). When the models are applied either to small rings or to ring rolling processes that are too fast, the underestimation in the prediction can reach 28%. For this reason, the process planner should apply these models with caution.

References

[1] G. Zhou, L. Hua and D.S. Qian, 3D coupled thermo-mechanical FE analysis of roll size effects on the radial–axial ring rolling process, Computational Material Science **50** (2011), 911–924.

[2] J.M. Alwood, A.E. Tekkaya and T.F. Stanistreet, The development of ring rolling technology, Steel Research International **76** (2005), 111–120.

[3] L. Guo and H. Yang, Towards a steady forming condition for radial–axial ring rolling, Int. Journal of Mechanical Sciences **53** (2011), 286–299.

[4] A. Parvizi, K. Abrinia and M. Salimi, Slab analysis of ring rolling process assuming constant shear friction, Journal of Materials Engineering and Performance **20** (2011), 1505–1511.

[5] A. Parvizi and K. Abrinia, A two-dimensional upper bound analysis of the ring rolling process with experimental results, Int. Journal of Mechanical Sciences **79** (2014), 176–181.

[6] J.B. Hawkyard, W. Johnson, J. Kirkland and E. Appleton, Analyses for roll force and torque in ring rolling, with some supporting experiments, Int. Journal of Mechanical Sciences **15** (1973), 873–893.

[7] A.G. Mamalis, W. Johnson and J.B. Hawkyard, Analyses for roll force and torque in ring rolling, with some supporting experiments, Journal of Mechanical Engineering Sciences **18:4** (1976), 196–208.

[8] G.A. Berti, L. Quagliato and M. Monti. Set-up of radial-axial ring-rolling process: Process worksheet and ring geometry expansion prediction, Int. Journal of Mechanical Sciences **99** (2015), 55–71.

[9] Quagliato L, Berti GA. Mathematical definition of the 3D strain field of the ring in the radial-axial ring rolling process, Int. Journal of Mechanical Sciences **115-116** (2016), 746–759.

[10] R. Hill, *The Mathematical Theory of Plasticity* (1950), Clarendon Press, Oxford.

[11] J.S. Ryoo and D.Y. Yang, The influence of process parameters on torque and load in ring rolling, Journal of Mechanical Working Technology **12** (1986), 307–321.

[12] M.M. Al-mohaileb, Computer Modelling of the Temperature Profile during the Ring Rolling Process, Ph.D. Thesis, Ohio University (2000).

[13] D.S. Qian, L. Hua and L.B. Pan, Research on gripping conditions in profile ring rolling of raceway groove, Journal of Material Processing Technology **209** (2009), 2794–2802.

[14] N. Kim, H. Kim and K. Jin, Optimal design to reduce the maximum load in ring rolling process, Int. Journal of Precision Engineering and Manufacturing, **13** (2012), 1821–1828.

[15] P. Mangonon and G. Thomas, Structure and properties of thermal-mechanically treated 304 stainless steel, Metall. Trans., Vol. 1, No. 6, pp. 1587-1594, 1970.

[16] A. Hensel, T. Spittel, Kraft - und Arbeitsbedarf bildsamer Formgebungsverfahren, 1st edition, Deutscher Verlag für Grundstoffindustrie (1978), Leipzig.

highlight

- Reliable lumped parameters heat exchange analytical model for the ring
- Analytical estimation of the radial forming force using slip-line field
- Validation of the models with FEM simulations and experiments
- Investigation of the influence of ring geometry on the force prediction
- Investigation of the influence of the mandrel speed on the force prediction

graphical abstract